Far-field diffraction microscopy at $\lambda/10$ resolution

Ting Zhang, Charankumar Godavarthi, Patrick C. Chaumet, Guillaume Maire, Hugues Giovannini, Anne Talneau, Marc Allain, Kamal Belkebir, Anne Sentenac

optica

Far-field diffraction microscopy at λ/10 resolution

Ting Zhang,[1] Charankumar Godavarthi,[1] Patrick C. Chaumet,[1] Guillaume Maire,[1] Hugues Giovannini,[1] Anne Talneau,[2] Marc Allain,[1] Kamal Belkebir,[1] and Anne Sentenac[1,*]

[1]Aix Marseille Université, CNRS, Centrale Marseille, Institut Fresnel, UMR 7249, 13013 Marseille, France
[2]CNRS, Laboratory for Photonics & Nanostructures, 91460 Marcoussis, France
*Corresponding author: anne.sentenac@fresnel.fr

Received 24 February 2016; revised 2 May 2016; accepted 13 May 2016 (Doc. ID 259996); published 7 June 2016

Tomographic diffraction microscopy is a three-dimensional quantitative optical imaging technique in which the sample is numerically reconstructed from tens of holograms recorded under different angles of incidence. We show that combining the measurement of the amplitude, the phase, and the polarization of the field scattered by the sample with an approximate knowledge of the sample permittivity allows reconstruction of spatially complex samples up to 50 nm resolution. This technique should be particularly useful for imaging objects made of known materials.

OCIS codes: (180.3170) Interference microscopy; (100.3200) Inverse scattering; (100.6640) Superresolution.

http://dx.doi.org/10.1364/OPTICA.3.000609

The resolution of diffraction microscopy is fundamentally limited by the elastic light–matter interaction. The Abbe limit states that, in the single scattering regime, the far field scattered by an object illuminated under propagative waves conveys information on the spatial frequencies of the sample permittivity distribution up to $2/\lambda$ at most (where λ is the illumination wavelength in the background medium). Now, the knowledge of the object spatial frequencies within a ball of radius $2/\lambda$ yields a spatial resolution, defined as the full width at half-maximum of the reconstruction of a point-like object, about 0.3λ [1]. In addition, this limit is far from being observed in practice with conventional microscopes, whatever their configuration (brightfield, darkfield, or even confocal) [2].

A widely explored approach for improving the resolution consists of taking advantage of evanescent waves for the illumination or the detection via near-field probes, metamaterial lenses, or plasmons [3–6]. These techniques ameliorate the resolution, albeit rarely further than 0.3λ in practice, but at the expense of an increase in experimental complexity and a restriction to surface imaging.

Another research avenue consists of extracting the most out of the sample scattered field using numerical reconstructions based on an accurate model of the sample–light interaction. The quantitative imaging approach has been implemented on many different far-field microscope configurations [7–11], which all aim at recovering the phase and amplitude of the field scattered by the sample for many incident angles, either directly with an interferometric mounting as in tomographic diffraction microscopy (TDM) [10–13] or indirectly via a ptychography-like technique [14,15]. In parallel, many reconstruction algorithms have been proposed to retrieve the sample permittivity distribution from measured scattered field data, from direct linear inversion [7,10,11] to iterative reconstruction schemes [12,14–16]. All these techniques exhibited a better resolution than that of equivalent analog microscopes, and ranged, in certain cases, up to 0.3λ [11–13,17].

To overcome this limit, one needs to address the fundamental issue of far-field imaging. When the target is much smaller than the wavelength, the scattered field depends mainly on the product of the object volume with the object permittivity contrast. Thus, in the presence of noise, its signature can be confused with that of a bigger object with a smaller permittivity contrast. We reasoned that setting the permittivity contrast to a given value, knowing the physical nature of the sample, would remove this indetermination and allow the retrieval of the accurate volume of the subwavelength target, hopefully way beyond the diffraction limit. In this work, we developed a sophisticated inversion technique, adapted to TDM data, that imposes a binary behavior to the sought permittivity distribution. We obtained an unprecedented $\lambda/10$ resolution on complex objects, experimentally.

Hereafter, we considered nanofabricated objects made of known material, deposited on a Si substrate. This particular geometry was chosen to approach the imaging issues encountered in the control of silicon wafers. The samples were imaged with a homemade off-axis holographic reflection microscope, yielding the phase and amplitude of the field at the image plane for plane-wave illuminations with varying incident angles. To obtain an isotropic resolution in the transverse plane, accounting for and taking advantage of the vectorial nature of light are mandatory [18]. Hence, four measurements corresponding to different polarization pairs of the incident and reference beams were carried out for each incident angle. The data were then calibrated, using the specular reflection beam as a phase and amplitude reference, and appropriately combined to form the vectorial far field $\mathbf{f}_{l,m}^{\text{mes}}$ scattered by the sample along $m = 1, \ldots, M$ directions of observation, $\mathbf{k}_m$, for $l = 1, \cdots, L/2$ directions of illumination, $\mathbf{k}_l$, and two independent incident polarizations. More details on the experimental mounting are given in Supplement 1.

All the experiments were conducted with $L = 44$ illuminations regularly spaced within a cone of polar angle $\theta_{max} = 63°$ and $M = 6361$ observation directions, regularly spaced within a cone of polar angle $\theta_{max} = 72°$. The wavelength of the illuminated laser beam was $\lambda = 475$ nm. With such numerical aperture and wavelength, the resolution of a conventional analogical microscope is estimated to $0.7\lambda \approx 330$ nm.

The permittivity distribution $\epsilon(\mathbf{r})$ within a bounded investigating domain Ω was reconstructed from the scattered far-field data using a reconstruction algorithm, hereafter called the bounded inversion method (BIM), which took advantage of the knowledge of the object and background relative permittivity values, ϵ_{ref} and $\epsilon_{background}$, respectively.

Few techniques have been proposed that enforce a binary behavior to the sought permittivity distribution [19,20]. Based on complex representations of the object, they usually require the tuning of numerous parameters and are significantly more time-consuming than nonconstrained inversion schemes. To our knowledge, they have not yet been applied to configurations with a large number of data such as that encountered in three-dimensional optical microscopy. In contrast, BIM requires minimal changes in a standard gradient minimization method and proves to be as fast as its unconstrained counterpart. It does not impose strictly the two values $\epsilon_{background}$ and ϵ_{ref} to the relative permittivity distribution, but rather boosts their apparition [21]. We start from a standard inversion scheme where the permittivity contrast $\chi(\mathbf{r}) = \epsilon(\mathbf{r}) - \epsilon_{background}$ in Ω is estimated iteratively by minimizing a cost functional $\mathcal{F}(\chi)$ [22] that represents the L2 distance between the experimental data $\mathbf{f}_{l,m}^{mes}$ and the field $\mathbf{f}_{l,m}^{sim}$ that would be scattered by the permittivity estimate:

$$\mathcal{F}(\chi) = \frac{\sum_{l=1}^{L}\sum_{m=1}^{M} \|\mathbf{f}_{l,m}^{mes} - \mathbf{f}_{l,m}^{sim}(\chi)\|^2}{\sum_{l=1}^{L}\sum_{m=1}^{M} \|\mathbf{f}_{l,m}^{mes}\|^2}. \quad (1)$$

For a given estimate χ, the scattered field $\mathbf{f}_{l,m}^{sim}$ is simulated rigorously using the coupled dipole method [22]. This technique ensures an accurate solving of Maxwell's equations and is able to account for multiple scattering, if any. To constrain the permittivity, the contrast χ is written in the form

$$\chi = (\epsilon_{ref} - \epsilon_{background})[1 - \exp(-\xi^2)], \quad (2)$$

where ξ became the novel parameter of the inversion algorithm. Using this formulation, small ξ corresponds to the background medium and large ξ corresponds to the object. At each iteration, ξ was modified along a descent direction that depended on the gradient of the cost function with respect to χ times the derivative of χ with respect to ξ. By construction, the descent direction tends toward 0 for small and large ξ, and thus promotes the extreme values $\epsilon_{background}$ or ϵ_{ref} for the estimated permittivity. A complete description of the coupled dipole method and the inversion scheme is provided in Supplement 1.

To stress the role of the binary constraint on the permittivity retrieval, we compared the BIM reconstructions to that given by another iterative inversion algorithm, named the hybrid method (HM), that assumes solely the positivity of the sought permittivity. HM has proven to be effective on numerous experimental data [12,23] and is also based on a rigorous solving of the Maxwell equations.

We first investigated the performance of the reconstruction schemes on synthetic data, and considered samples with identical geometry but different permittivities that were belonging either to the weak or moderate scattering regimes. To ensure the same signal-to-noise ratio in both cases, the scattered far field was corrupted with a multiplicative white random noise of root mean square 10%. The samples were made of three cubes of side $\lambda/20$ placed at the summits of an isosceles triangle with center interdistances $\lambda/10$ and $\lambda/9$. The background was air, $\epsilon_{background} = 1$.

In the first example, the object permittivity $\epsilon_{ref} = 1.01$ was taken close enough to that of the background for the single scattering approximation to be valid. In this regime, the data are blind to any object spatial frequency larger than $2/\lambda$, and the resolution accessible without any *a priori* information is $\lambda/3$ which is much bigger than the cubes' interdistances. It was hoped that by restraining the set of possible outcomes of the inversion schemes using some information on the target permittivity, the recovery of object high spatial frequencies beyond that physically accessible could occur. However, it was observed in Fig. 1(a) that the sole positivity constraint of HM failed to ameliorate the reconstruction beyond the accessible Fourier domain. BIM provided a better reconstruction than HM, yet still without distinguishing the three cubes [Fig. 1(b)]. In this case, the misfit between the data and the field scattered by the smooth permittivity estimate was so low (compared to the noise strength) that the BIM minimization process stopped before the reconstructed permittivity reached the targeted values ϵ_{ref} or $\epsilon_{background}$.

In the second example, the cubes' permittivity ϵ_{ref} was taken equal to 4. With such a permittivity contrast, the far-field data cannot be modeled using the single scattering approximation. so that the scattered far field depends formally on all the sample spatial frequencies [24,25]. This dependence can be an asset for inversion schemes that are based on a rigorous simulation of the light–matter interaction, and resolution beyond the Abbe limit

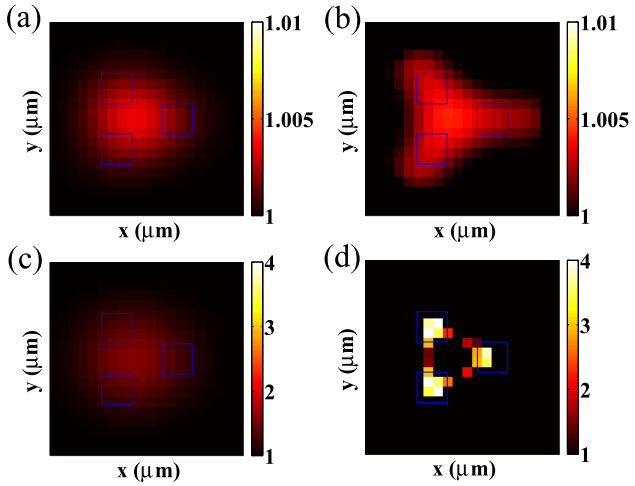

Fig. 1. Reconstruction of three cubes of side $\lambda/20$ and center-to-center distance $\lambda/10$ and $\lambda/9$ from synthetic data corrupted with 10% multiplicative noise. In (a) and (b), the cubes' permittivity is 1.01. The single scattering approximation is valid. (a) Permittivity reconstruction obtained with HM using the positivity constraint. (b) Permittivity reconstruction with the BIM using the knowledge of target permittivity. (c) and (d) are same as (a) and (b), but the permittivity of the cubes is 4 and the single scattering approximation is no longer valid. BIM is always better than HM and is able, in the multiple scattering regime, to retrieve accurately the three cubes way beyond the Rayleigh limit. The mesh size of the reconstruction is $\lambda/60$.

has been observed in the multiple scattering regime [24–26]. However, because the inverse problem is nonlinear, the convergence toward an accurate estimate is not always ensured [27].

In the present case, despite the presence of multiple scattering and its ability to account for it, HM failed in distinguishing the three cubes [Fig. 1(c)]. In contrast, BIM provided an accurate description of the sample with a reconstructed permittivity reaching 4 [Fig. 1(d)]. The better resolution of BIM reconstruction in the multiple scattering regime can be explained by noting that the particular expression of the sought permittivity promotes, by construction, permittivity distribution with high spatial frequencies. When the latter have an impact on the far-field data, thanks to multiple scattering, they are likely to be better estimated.

We now turn to the reconstruction of several samples from experimental data. We considered a star sample made of 12 resin rods ($\epsilon_{\text{ref}} = 2$), of length 520 nm, width about 97 nm, and height 140 nm, touching each other at the center of the star [Fig. 2(a)]. Note that the spacing between the rods is always inferior to the resolution of a conventional analogical microscope, even at the external border, where it reaches 320 nm. Despite a moderate contrast and small 140 nm height, we observed with rigorous simulations that such a sample supports multiple scattering. The BIM reconstruction obtained from these synthetic data prove to be perfect, as shown in Supplement 1. In the experiment, however, the data were significantly corrupted by noise, stemming essentially from calibration errors and unwanted speckle. The latter was estimated, by replacing $\mathbf{f}_{l,m}^{\text{sim}}(\chi)$ by $\mathbf{f}_{l,m}^{\text{sim}}(\chi_{\text{true}})$ in Eq. (2), at about 55%.

To reduce the influence of the speckle noise, we processed the data with an efficient approach based on the singular value decomposition of the scattering matrix [28]. Basically, we formed linear combinations of $\mathbf{f}_{l,m}^{\text{mes}}$ in order to generate the target responses to specific illuminations that are focused on the target; see Supplement 1 for more detail. The inversion procedure was then applied to these rearranged data.

We first examined the target using classical microscopy. As expected, the darkfield microscope image [Fig. 2(b)] obtained by summing the diffracted intensities recorded at the image plane for all the illuminations retrieved a doughnut without any hint about the rods. The standard tomographic reconstruction (using a Fourier transform technique for processing the data [1,7,13]), did not show any marked improvement (not shown). In contrast, the rods were visible up to mid-length on the HM reconstruction [Fig. 2(c)] and were dramatically retrieved on the BIM reconstruction [Fig. 2(d)]. More precisely, the air wedge between the resin branches could be retrieved by HM down to 150 nm and by BIM down to 50 nm.

To push further the investigation on the limits of our imager, we considered in a second example a star sample made of rods of width 76 nm, length about 490 nm, and height 140 nm [Fig. 3(a)]. With this smaller and less scattering sample, the experimental noise was estimated at about 85%. Unsurprisingly, classical microscopy and standard tomography failed to image the sample [Fig. 3(b)]. On the other hand, the rods started to be visible in the HM reconstruction [Fig. 3(c)] and were retrieved up to their contact point by BIM [Fig. 3(d)]. In this noisier experiment, the air wedge between the branches could be retrieved by HM down to 200 nm and by BIM down to 50 nm, which emphasizes the robustness of the reconstruction procedure. The axial reconstruction of the 76 nm star was, however, more imprecise

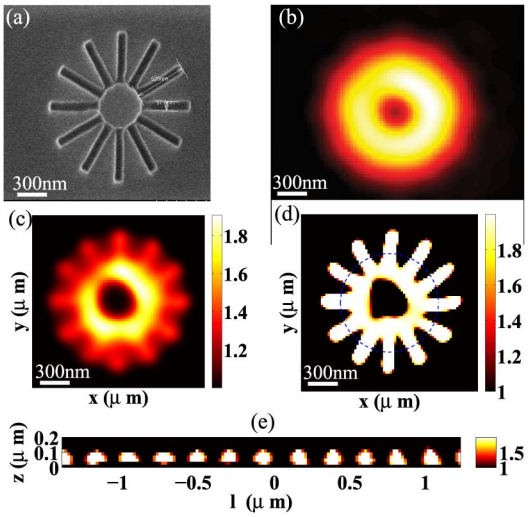

Fig. 2. Images of a resin star sample of 97 nm wide rods of length 520 nm and height 140 nm on a Si substrate. (a) Scanning electronic microscope image. (b) Darkfield microscopy with NA = 0.95. (c) Reconstruction obtained with HM from tomographic diffraction microscopy data with NA = 0.95. (d) Permittivity reconstruction obtained with BIM using the knowledge of the resin permittivity from the same data as (c). (e) Permittivity distribution in the axial z direction versus the curvilinear abscissa of the dashed circle in (d). The mesh size taken for all the reconstructions is 20 nm. BIM is able to distinguish the rods down to an interspacing of about 50 nm. The width of the rods is estimated to 117 nm in average (between 5 and 6 pixels). The color code indicates the level of relative permittivity in (c) and (d).

than that of the 97 nm star, as shown on the three-dimensional isocontours of the reconstrutions displayed in Supplement 1.

Most impressively, BIM was able to distinguish rods of width 97 nm from rods of width 76 nm; compare Figs. 2(d) and 3(d). The average values of the reconstructed rod width, measured at mid-length over all the branches, was 117 nm for the first sample and 87 nm for the second one. This result is in agreement with the air wedge retrieval and suggests that, on these examples, the

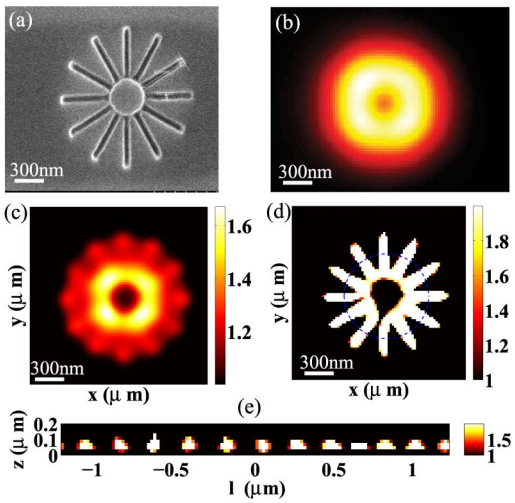

Fig. 3. Same as Fig. 2, but the rod width is 76 nm and their length is 490 nm. BIM is able to distinguish the rods down to an interspacing of about 50 nm. The rods' width is estimated to 87 nm on average (between 4 and 5 pixels).

resolution of BIM was about 50 nm, if not better. Note, however, that defining a resolution limit in a nonlinear imaging experiment using *a priori* information is a difficult task as, in addition to noise, it depends on the scattering regime and on the unknown-over-data ratio [29,30].

In conclusion, a resolution of at least one-tenth of the wavelength was observed experimentally on complex samples with a tomographic diffraction microscope using an inversion procedure that accounts for multiple scattering and an approximate knowledge of sample permittivity. This development should find many applications in the nanotechnology and solid-state domains, and, more generally, in all cases in which the samples are made of known materials.

Funding. Agence Nationale de la Recherche (ANR) (SURMITO).

See Supplement 1 for supporting content.

REFERENCES

1. O. Haeberlé, K. Belkebir, H. Giovaninni, and A. Sentenac, J. Mod. Opt. **57**, 686 (2010).
2. G. Cox and C. J. R. Sheppard, Microsc. Res. Tech. **63**, 18 (2004).
3. E. Betzig, J. K. Trautman, T. D. Harris, J. S. Weiner, and R. L. Kostelak, Science **251**, 1468 (1991).
4. Z. Liu, H. Lee, Y. Xiong, C. Sun, and X. Zhang, Science **315**, 1686 (2007).
5. J. Rho, Z. Ye, Y. Xiong, X. Yin, Z. Liu, H. Choi, G. Bartal, and X. Zhang, Nat. Commun. **1**, 143 (2010).
6. B. Gjonaj, J. Aulbach, P. M. Johnson, A. P. Mosk, L. Kuipers, and A. Lagendijk, Phys. Rev. Lett. **110**, 266804 (2013).
7. V. Lauer, J. Microsc. **205**, 165 (2002).
8. S. A. Alexandrov, T. R. Hillman, T. Gutzler, and D. D. Sampson, Phys. Rev. Lett. **97**, 168102 (2006).
9. V. Mico, Z. Zalevsky, P. Garcia-Martinez, and J. Garcia, J. Opt. Soc. Am. A **23**, 3162 (2006).
10. Y. Sung, W. Choi, C. Fang-Yen, K. B. Zadegan, R. R. Dasari, and M. S. Feld, Opt. Express **17**, 266 (2009).
11. M. Debailleul, V. Georges, B. Simon, R. Morin, and O. Haeberlé, Opt. Lett. **34**, 79 (2009).
12. T. Zhang, Y. Ruan, G. Maire, D. Sentenac, A. Talneau, K. Belkebir, P. C. Chaumet, and A. Sentenac, Phys. Rev. Lett. **111**, 243904 (2013).
13. Y. Cotte, F. Toy, P. Jourdain, N. Pavillon, D. Boss, P. Magistretti, P. Marquet, and C. Depeursinge, Nat. Photonics **7**, 113 (2013).
14. L. Tian and L. Waller, Optica **2**, 104 (2015).
15. G. Zheng, R. Horstmeyer, and C. Yang, Nat. Photonics **7**, 739 (2013).
16. U. S. Kamilov, I. N. Papadopoulos, M. H. Shoreh, A. Goy, C. Vonesch, M. Unser, and D. Psaltis, Optica **2**, 517 (2015).
17. C. Godavarthi, T. Zhang, G. Maire, P. C. Chaumet, H. Giovannini, A. Talneau, K. Belkebir, and A. Sentenac, J. Opt. Soc. Am. A **32**, 287 (2015).
18. G. Maire, Y. Ruan, T. Zhang, P. C. Chaumet, H. Giovannini, D. Sentenac, A. Talneau, K. Belkebir, and A. Sentenac, J. Opt. Soc. Am. A **30**, 2133 (2013).
19. A. Litman, D. Lesselier, and F. Santosa, Inverse Probl. **14**, 685 (1998).
20. H. Ayasso, B. Duchêne, and A. Mohammad-Djafari, J. Mod. Opt. **57**, 765 (2010).
21. P. C. Chaumet, K. Belkebir, and A. Sentenac, J. Appl. Phys. **106**, 034901 (2009).
22. T. Zhang, P. C. Chaumet, E. Mudry, A. Sentenac, and K. Belkebir, Inverse Probl. **28**, 125008 (2012).
23. E. Mudry, P. C. Chaumet, K. Belkebir, and A. Sentenac, Inverse Probl. **28**, 065007 (2012).
24. F. Simonetti, Phys. Rev. E **73**, 036619 (2006).
25. K. Belkebir, P. C. Chaumet, and A. Sentenac, J. Opt. Soc. Am. A **23**, 586 (2006).
26. J. Girard, G. Maire, H. Giovannini, A. Talneau, K. Belkebir, P. C. Chaumet, and A. Sentenac, Phys. Rev. A **82**, 061801 (2010).
27. A. Litman and L. Crocco, Inverse Probl. **25**, 020201 (2009).
28. T. Zhang, C. Godavarthi, P. C. Chaumet, G. Maire, H. G. Nnini, A. Talneau, C. Prada, A. Sentenac, and K. Belkebir, Opt. Lett. **40**, 573 (2015).
29. J. Qin, R. M. Silver, B. M. Barnes, H. Zhou, R. G. Dixson, and M.-A. Henn, Light Sci. Appl. **5**, e16038 (2016).
30. A. Sentenac, C.-A. Guérin, P. C. Chaumet, F. Drsek, H. Giovannini, N. Bertaux, and M. Holschneider, Opt. Express **15**, 1340 (2007).